Hidden symmetries in bowtie nanocavities and diabolo nanoantennas

Victor Pacheco-Peña[†,*], *Rúben Alves*[Ω] *and Miguel Navarro-Cía*[Ω,*]

[†]School of Engineering, Newcastle University, Merz Court, Newcastle Upon Tyne NE1 7RU, UK.

[Ω]School of Physics and Astronomy, University of Birmingham, Birmingham B15 2TT, UK
m.navarro-cia@bham.ac.uk

*victor.pacheco-pena@newcastle.ac.uk Phone: +44(0)1912088665
*m.navarro-cia@bham.ac.uk Phone: +44(0)1214144664; Fax: +44(0)1214144644

KEYWORDS: Conformal mapping, bowtie nanoantenna, nanocavity, suface plasmons, hidden symmetry

ABSTRACT: Symmetries play an important role in many branches of physics and enable simplification of the mathematical description of problems. In some cases, symmetries are hidden and are only evident under suitable coordinate systems. With the help of conformal transformation, it is shown analytically here how asymmetric-looking plasmonics diabolo nanoantennas and bowtie nanocavities display a hidden symmetry that justifies the unforeseen symmetric nonradiative Purcell enhancement of a nanoemitter in their immediacy. The conformal transformation also provides physical insight on the dissimilar self-induced trapping potential experienced by such nanoemitter nearby/inside the diabolo nanoantenna/bowtie nanocavity. The analytical results are confirmed with full-wave simulations. This work highlights the elegant and cost-effective (in terms of computational burden) solution that conformal transformation provides to understand the underlying physics of and to design/model plasmonic nanostructures that are becoming key elements in sensing, quantum optics, etc.

Within the past few years, the field of plasmonics has advanced in unprecedented steps offering groundbreaking opportunities in different fields ranging from spectroscopy [1,2], focusing and beam steering devices [3,4] and biomedical applications [5,6]. This has been possible because of the high near-field concentration of electromagnetic fields enabled by metal-dielectric plasmonic nanostructures working at nanometer-scaled wavelengths via localized surface plasmons (LSPs) [7–11]. Interestingly, this large and enhanced field concentration occurs within (sub-)nanometric volumes, a feature that has been exploited in order to overcome the diffraction limit of imaging systems [12–14] and also to design optical nanotweezers [15–17]. Furthermore, it has been shown how plasmonic nanostructures can be applied to enhance nonlinear effects [18–22].

In this realm, plasmonic nanoantennas [23–27], in particular bowtie geometries, have become popular because of the broadband field enhancement and nanoscale confinement achieved at their apex [28–32]. Additionally, attention has been also given to plasmonic bowtie nanocavities

for nanolithography [33,34], single molecule fluoresce [35] and optical trapping [28,36] because of the background-free illumination provided by the nanoaperture.

Similar to low frequency (radio, microwave, millimeter waves) antennas and cavities (or apertures), the electromagnetic response of both plasmonic nanoantennas and nanocavities strongly depends on the materials, geometry, type of illumination (planewave, dipole, Gaussian beam), polarization, etc. [379,38]. Unlike at microwaves though, plasmonic nanoantennas and nanocavities designers need to account for the strong dispersive response of metals. Giving the complexity, the industry standard to design, model, grasp physical insight and understand experimental results is by implementing numerical full-wave simulations which require large computational resources [39].

Computational burden can be reduced with analytical solutions. In this context, transformation optics has demonstrated to be a useful tool to understand and model analytically the response of plasmonic nanostructures [40–43], including nanocrescent, cylinders, spheres, dimers tripods and bowtie nanostructures [27,28,44–50], that cannot be treated analytically otherwise. In this technique, the spatial coordinates of a nanoparticle is transformed into a different geometry which can be treated analytically even for dispersive materials. Interestingly, this conformal mapping can be used several times in a cascaded fashion, to draw the common underlying physics among at first sight completely different nanoparticles and to study rather complex geometries [45]. Indeed, conformal mapping has been recently applied to unveil hidden symmetries between geometrically-different nanoparticles [51], demonstrating how they can share the same spectral response. This knowledge has significant implications as far as physical understanding and design are concerned [8,51].

Motivated by the opportunities offered by plasmonic bowtie nanostructures, and the importance of symmetry in nanophotonics [51–53], in this manuscript we report for the first time a hidden geometrical symmetry (that is not related to Babinet's principle) between bowtie nanoantennas with connected arms (from now on called diabolo nanoantennas) and bowtie

nanocavities using the conformal transformation technique. Such hidden geometrical symmetry justifies the similar spectral response in terms of nonradiative Purcell enhancement (parameter here used as a figure of merit) and the asymmetric trapping potential experienced by a nanoemitter nearby/inside the diabolo nanoantenna/bowtie nanocavity. Also, this manuscript provides a comprehensive study of the influence of the diabolo/bowtie apex angle, polarization and location of the nanoemitter on the spectral response of the plasmonic system. All the results are corroborated with numerical simulations demonstrating a good agreement with the analytical values.

RESULTS AND DISCUSSION

Purcell enhancement

To begin with, let us consider the diabolo nanoantenna and bowtie nanocavity shown as insets in Figure 1, which are invariant out-of-plane. They are defined by the length of the arm, $L'_1 + L'_2$, the arm angle θ' and the Ø1 nm metallic circular patch (air gap) connecting (separating) the two arms for the diabolo nanoantenna (bowtie nanocavity), see Figure 2a,c for visual definition of the parameters. The total length l' corresponds to the arms' length $2(L'_1 + L'_2)$ along with the 1 nm patch (gap) for the diabolo nanoantenna (bowtie nanocavity). For the bowtie nanocavity, the outer ring width is selected to be $\Delta' t$ = 10 nm in order to consider it as an aperture in a semi-infinite metal [28]. Gold is used as the metal for all nanoparticles, which are illuminated with a localized emitter placed at (x' = 1 nm, y' = 0 nm).

Figure 1a,b and Figure 1c,d show the Comsol® full-wave simulation results of the nonradiative Purcell enhancement (defined as the absorbed power by the nanoparticle relative to the radiated by the nanoemitter) considering different values of θ' (20° and 45°) and polarization of the nanoemitter for the diabolo nanoantenna and bowtie nanocavity, respectively. Several peaks are obtained within the spectral band under study, which are related to each LSP mode (n = 1,2,…) excited in the nanoparticles [46,54]. Remarkably, the responses of

both nanoparticles are rather similar. For instance, under vertical polarization (Figure 1a,c) the LSP mode of order $n = 1$ for the bowtie nanoantenna with $\theta' = 20°$ appears at the wavelength of ~882 nm while it is at ~909 nm for the nanocavity. Under horizontal polarization (Figure 1b,d) the fundamental LSP mode for the $\theta' = 20°$ bowtie nanoantenna is obtained at ~600 nm, exactly the same value as the bowtie nanocavity. Similar results are obtained for the nanoparticles with $\theta' = 45°$ where the LSP mode with $n = 1$ is located at ~714 nm and ~750 nm for the nanoantenna and nanocavity, respectively, under vertical polarization of the nanoemitter. For the horizontal polarization, the fundamental LSP mode appears squarely at ~535 nm for both nanostructures.

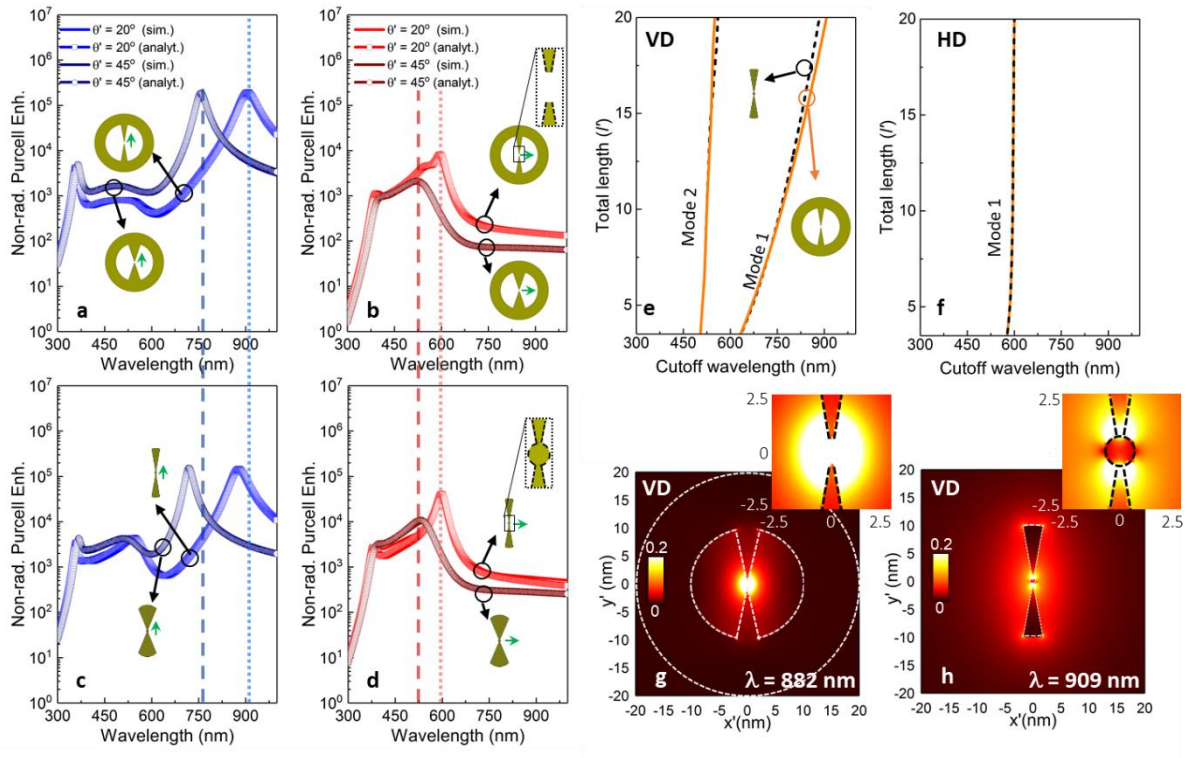

Figure 1. Analytical (symbols) and numerical results (solid lines) results of the $\overline{\Gamma_{nr}}$ for $l' = 20$ nm bowtie nanocavities (a,b) and diabolo nanoantennas (c,d) with $\theta' = 20°$ (light) and $\theta' = 45°$ (dark) under vertical (a,c) and horizontal (b,d) polarization of the nanoemitter. (e) Cut-off wavelength of the LSP modes with $n = 1$ and 2 for a diabolo nanoantenna (black dashed line) and bowtie nanocavity (orange solid line) with $\theta' = 20°$ when the length l' is changed under vertical polarization of the nanoemitter. (f) The same as (e) for the fundamental LSP mode under horizontal polarization of the nanoemitter. Normalized magnitude of the electric field at

the wavelength of the fundamental LSP mode for the bowtie nanocavity (g) and diabolo nanoantenna (h) under vertical polarization of the nanoemitter.

A parametric sweep of the size of the nanostructures (Figure 1e,f) reveals that the electromagnetic behavior of both geometries in terms of nonradiative Purcell enhancement converge as the size is reduced (i.e. when the nanoparticles fall well within quasi-static limit), despite the completely different field distribution of the modes (see Figure 1g,h where the distributions of the normalized magnitude of the electric field for the LSP mode of $n = 1$ are shown considering nanoparticles with $\theta' = 20°$ under vertical polarization of the nanoemitter). As it will be further explained in the following sections, the different field distribution produced by each nanostructure will generate different spatial field gradients. Hence, a nanoemitter illuminating the diabolo nanoantennas and bowtie nanocavities will experience a different self-induced trapping potential. However, despite their different spatial distribution of their LSP modes, both nanostructures have a symmetric spectral response in term of nonradiative Purcell enhancement, as shown before. It is important to note that this hidden symmetry in terms of nonradiative Purcell enhancement between both nanostructures is not the general property of local plasmons observed in simple metal nanostructures [55] and is not related to the Babinet's principle in complementary structures [56]. Unlike Babinet's principle conditions, here a 2D problem is evaluated (i.e., out-of-plane invariant nanostructures), the symmetric behavior occurs for the same polarization, the nanoparticles are not complementary in the original space (see Figure S3 in the supplementary information for more details) and the metal used is a dispersive material (not perfect electric conductor, PEC).

What is the reason behind this unexpected symmetric response? The following section will answer this question with the aid of conformal transformation.

Analytical approach

From now on, we will only consider realistic nanostructures with total length of l' = 20 nm. Smaller l' would leave to feature sizes challenging for current nanofabrication technologies [57]. Note that l' = 20 nm enables us to invoke the quasi-static approximation for the analytical analysis. Hence, the magnetic and electric fields are decoupled and the latter can be expressed via an electrostatic potential satisfying Laplace's equation. Additionally, since the size of the bowtie nanocavities and diabolo nanoantennas under study are smaller than the illuminating wavelength ($l' << \lambda_0$), radiation losses are negligible and it can be considered that the energy radiated by the nanoemitter is absorbed by the metallic nanoparticles [54]. The quasi-static limit is a useful and pertinent approximation for many plasmonic systems. Within this quasi-static limit, it has been previously reported that largely different geometrical objects can have the same far-field optical properties for the fundamental LSP mode [55]. In the present work, we go beyond this finding and show, with the help of conformal transformation, the role that near-field interactions play, and thus, the key influence of the nanoemitter's polarization and location with respect to the different LSP modes.

As shown in Figure 2a,c, the spatial coordinates of the diabolo nanoantenna and bowtie nanocavity are $z' = x' + iy'$. Here $z = x + iy$ are the spatial coordinates of the transformed frames. By applying the transformation $z = \ln(z'/a)$, the nanostructures and the line dipole nanoemitter are transformed into the periodic multislab geometries shown in Figure 2b,d with a periodicity of 2π along the y axis. From this figure, it is interesting to note how the periodic multislabs in the transformed space for both nanoparticles (nanoantenna and nanocavity) are connected in one of the extremes while they are disconnected at the opposite end meaning that both nanoparticles are transformed into the same geometry after the conformal mapping is applied. Hence, even when both nanostructures are asymmetric in the original frame (z'), they have a hidden symmetry (mirror symmetry in this case) that can be retrieved from the transformed geometry. Notice that the total systems will be exactly mirror symmetric provided

the nanoemitter is in different locations in the original frame. This explains why the diabolo nanoantennas and bowtie nanocavities from Figure 1 have rather similar spectral response. It is worth re-emphasizing the key impact of the aforementioned hidden symmetry by looking at another geometry, namely the diabolo nanocavity, that introduces a minor modification (compared to the bowtie nanocavity) in the form of a Ø1 nm gold patch at the center. One could have argued that such minor inclusion should have had negligible influence in the nonradiative Purcell enhancement. However, on the contrary, it results into a significant red-shift (~200 nm shift) of the fundamental peak as shown in Figure S1 of the Supplementary Information, which can be explained by looking at the transformed space and the absence of mirror symmetry compared to the two nanostructures considered in the main body of this manuscript.

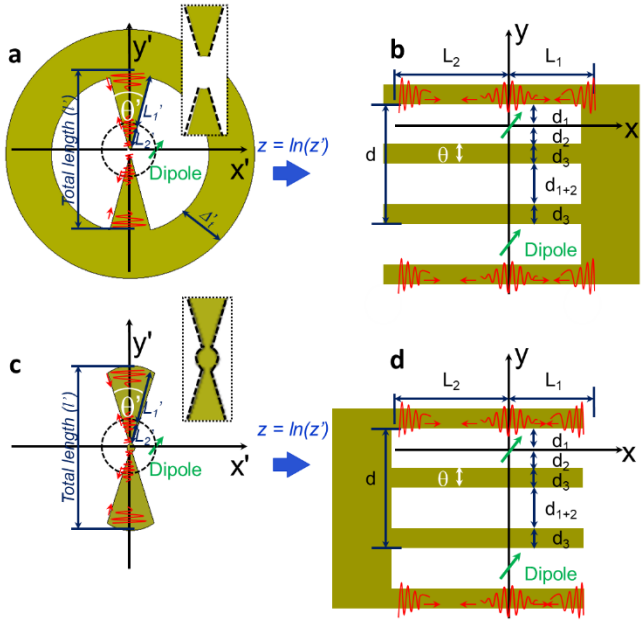

Figure 2. Schematic representation of the Gap bowtie nanocavity (a) and diabolo nanoantenna (b) along with their corresponding transformed multislab geometries (b and d, respectively) after applying the conformal mapping technique.

Due to the conformal mapping and the quasi-static treatment, the material properties and potentials $\varphi(x,y) = \varphi(x',y')$ are preserved in both z and z' scenarios, and thus, the dissipated

power is identical in both original and transformed frames $P_{abs}^{(x\prime,y\prime)} = P_{abs}^{(x,y)}$. In the multislab geometry, it can be calculated as $P_{abs}^{(x,y)} = P_{nr} = -(1/2)\omega\{p_x^* E_{1x}^S(x,y) + p_y^* E_{1y}^S(x,y)\}$ where P_{nr} is the nonradiative power emission, ω is the angular frequency, p_x and p_y are the components of the dipole moment with magnitude $|\,p\,|$ and $E_{1x}^S(x,y)$ and $E_{1y}^S(x,y)$ are the components of the electric field within the spatial region where the line dipole source is present (see Figure 2 and Methods section for more details). The power radiated by the nanoemitter can be calculated as $P_0 = -(1/16)\omega^3\mu_0|p|^2$ with μ_0 as the permeability in free space. Finally, the nonradiative Purcell enhancement can be analytically calculated as $\overline{F_{nr}} = P_{nr}/P_0$. In all the calculations here shown, an intrinsic quantum yield of 1 is used for the emitter in order to relate the nonradiative decay of the emitter with the power absorbed by the diabolo nanoantennas and bowtie nanocavities [28]. The complete analytical solution can be found in the Methods section. Based on this, the analytical results of the nonradiative Purcell enhancement for both diabolo nanoantennas and bowtie nanocavities considering θ' = 20° and θ' = 45° under vertical and horizontal polarization of the nanoemitter are also shown as symbols in Figure 1, where an agreement with the numerical calculations is observed. A small discrepancy of ~3% can be observed between the nanoantennas and nanocavities for the vertical polarization in Figure 1a,c though, which fades away as the l' is reduced (Figure 1e). Given the orientation of the nanoemitter with respect to the multislab geometry, the vertical polarization favors radiation compared to the horizontal polarization, as section 'Moving the nanoemitter along x' axis' will demonstrate. Thus, the limit of the quasi-static treatment is more stringent for the vertical polarization and our initial assumption $P_{abs}^{(x,y)} = P_{nr}$ starts to break down.

Although all the above and subsequent findings are for nanostructures that are invariant in the third dimension, the knowledge gained is directly applicable to real-world scenarios (i.e. nanostructures that are not invariant in the third dimension). To highlight this, several 1 nm thick nanocavities and diabolo nanoantennas illuminated by a nanoemitter were numerically

evaluated for different nanoemitter's polarizations, see Figure S2 in the Supplementary Information. The peaks of nonradiative Purcell enhancement for the 1 nm thick nanoantennas and corresponding nanocavities were found at the same wavelengths, in agreement with the findings of the main body of this manuscript for nanostructures that are invariant in the third dimension.

Self-induced trapping potential

To further evaluate the hidden symmetry present in both nanostructures, it is also interesting to discuss the self-induced trapping potential experienced by the nanoemitter when illuminating both diabolo nanoantennas and bowtie nanocavities. As it was discussed in Figure 1, both nanoparticles share the same spectral response because of the effect of the hidden mirror symmetry. However, as shown in Figure 1g,h, the field distribution for the LSP modes is different for each nanostructure. Hence, it could be expected different spatial distributions of self-induced trapping potential with both nanoparticles due to the fact that this parameter depends on the spatial distribution of the electric field for each LSP mode[28]. To evaluate this, a line colloidal ZnO quantum dot (QD) with a diameter of 2 nm [28,58] is considered as the nanoemitter. A diabolo nanoantenna and bowtie nanocavity with $\theta' = 20°$ is considered and filled with water ($\varepsilon_r = 1.77$) and the QD is moved within this aqueous region on the (x',y') plane. The potential energy of the ZnO QD when illuminating the nanostructures is evaluated as $V_{pot}(z') = -\int\langle F(z_1)dz_1\rangle$ where $\langle F\rangle$ is the optical force calculated using the Maxwell stress tensor from the field distribution of each LSP mode. As in [28], V_{pot} is normalized to k_BT (k_B and $T = 300K$ as the Boltzmann constant and temperature, respectively) in order to take into account the Brownian motion because of the aqueous medium where the ZnO QD is located.

With this setup, the results of the self-induced potential experienced by the QD for the LSP mode of order $n = 1$ are shown in Figure 3a,b and Figure 3c,d considering a diabolo nanoantenna and bowtie nanocavity, respectively. For completeness, both vertical and horizontal

photoluminescence are considered, as shown in the first and second column of the same figure, respectively. From these results, similar to the different electric field distribution discussed in Figure 1g,h, a clear difference in the distribution of the self-induced trapped potential is obtained when considering the diabolo nanoantenna and bowtie nanocavity. In the former case, the potential increases close to the center of the nanoparticle and decreases when the QD is moved away from this position with an almost zero value at x' = 9.6 nm (red color in Figure 3a,b). For the bowtie nanocavity, the potential is also increased for positions close to the center and it is reduced when it is moved away (see x' = 5 nm in Figure 3c,d). However, once the QD is moved closer to the external metallic ring the self-induced trapping potential is increased again (purple region in Figure 3c,d at x' = 9.6 nm). These results are in agreement with previous findings where it is expected to obtain a stable self-induced trapping potential close to the metallic regions and mainly at the center of the bowtie nanoantennas and nanocavities where the field gradient is higher [9,28]. Hence, despite the fact that both nanostructures have the same spectral response in terms of the cut-off frequency of the LSP modes (as shown in Figure 1), the trapping potential experienced by the QD will also depend on its location when illuminating the nanoparticles.

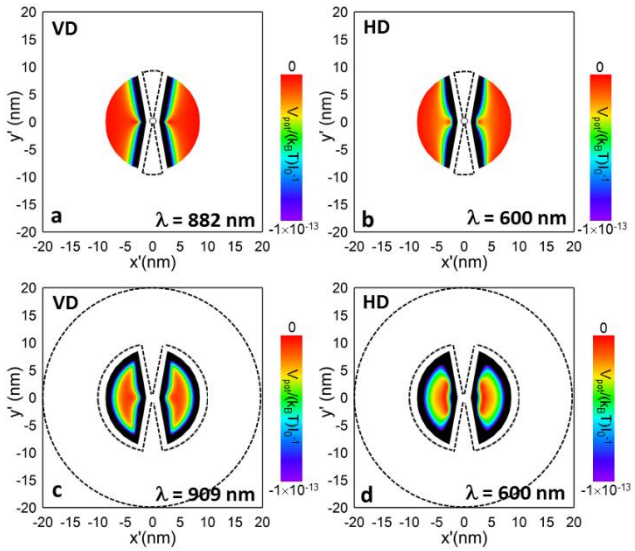

Figure 3. Normalized self-induced trapping potential distribution considering a ZnO colloidal QD with a diameter of 2 nm located inside of a diabolo nanoantenna (a,b) and bowtie nanocavity (c,d) with θ' = 20°, photoluminescence polarized vertically (a,c) and horizontally (b,d).

This performance can also be analytically described in terms of the different LSP modes excited in both diabolo nanoantenna and bowtie nanocavity. In the analytical approach, the LSP modes in the transformed multislab geometry (Figure 2c,d) are discretely distributed in the spectrum. This is due to the fact that the nanostructures under study have finite dimensions. Hence, it is possible to calculate the number of modes excited in each nanoparticle as well as their cut-off wavelength (see Methods section for more details). The analytical results of the number of LSP modes supported by both diabolo nanoantenna and bowtie nanocavity with $\theta' = 20°$ are shown in Figure 4a,b, respectively, for both vertical and horizontal polarization of the nanoemitter. As observed, higher number of modes are supported by the nanocavity compared to the nanoantenna for both polarizations of the nanoemitter. These higher order modes create field gradients which are then translated into zones of high self-induced trapped potential at the metal-dielectric interfaces [9,28]. This performance explains why there are more trapping regions with the nanocavity compared to the nanoantenna (as described before in Figure 3). For the sake of completeness, the analytical results of the cut-off wavelength for diabolo nanoantennas and bowtie nanocavities with $\theta' = 20°$ and $\theta' = 45°$ are shown in Figure 4c,d under vertical and horizontal polarization of the nanoemitter, respectively. A clear symmetric response is also obtained between both nanostructures and the modes of order $n > 3$ are agglomerated close to the SP wavelength (λ_{SP}).

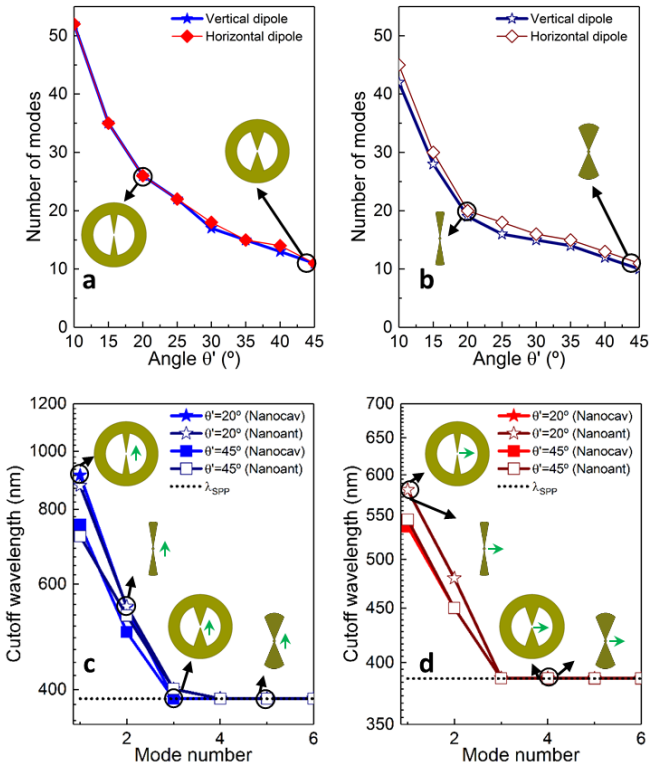

Figure 4. Number of LSP modes supported by the bowtie nanocavities (a) and diabolo nanoantennas (b) of different angular apertures θ' when they are illuminated using a nanoemitter with vertical (blue) and horizontal (red) polarization. (c,d) Analytical cut-off wavelength for bowtie nanocavities (solid symbols) and nanoantennas (white filled symbols) with $\theta' = 20°$ (stars) and $\theta' = 45°$ (squares) under vertical (c) and horizontal (d) polarization of the nanoemitter.

Moving the nanoemitter along the *x'* axis

In this section the influence of the location of the line dipole source along the x' axis is studied. The nanoemitter is moved from $x' = 0.8$ nm to $x' = 9.7$ nm with a step of $\Delta x' = 0.1$ nm. The diabolo nanoantenna and bowtie nanovavity (with $\theta' = 20°$) are studied under both vertical and horizontal polarization of the nanoemitter (see schematics in the first row of **Figure 5**). The analytical results of the $\overline{\Gamma_{nr}}$ spectra as a function of the nanoemitter location along the x' axis are shown in the second row of Figure 5. The numerical results of the $\overline{\Gamma_{nr}}$ are also shown in the third row from the same figure demonstrating a good agreement with the analytical values. As it is shown, the same trend as the case of the self-induced trapping potential experienced by the

QD (Figure 3) is obtained. For instance, under vertical polarization of the nanoemitter (first and second column of Figure 5) the $\overline{\Gamma_{nr}}$ of the fundamental LSP mode of order $n = 1$ for both bowtie nanocavity increases for positions close to their center and near the external metallic ring while it decreases in between these two extremes ($x' \sim 6.4$ nm), see Figure 5e,i. On the other hand, for the diabolo nanoantenna, the $\overline{\Gamma_{nr}}$ for the same LSP mode is also increased for positions of the nanoemitter near its center but it is reduced when it is moved away along the x' axis, Figure 5f,j. The same performance is obtained under the horizontal polarization of the nanoemitter for both bowtie nanocavity and diabolo nanoantenna (Figure 5g,k and Figure 5h,i, respectively).

For completeness, the numerical results of the radiative Purcell enhancement ($\overline{\Gamma_r}$) as a function of position of the nanoemitter along the x' axis are shown in the fourth row of Figure 5 for both nanoparticles under vertical and horizontal polarization of the line dipole source. The $\overline{\Gamma_r}$ is calculated as the ratio between the power scattered by the nanoparticle and that radiated by the nanoemitter alone ($\overline{\Gamma_r} = P_r/P_0$) [27,28,54]. The $\overline{\Gamma_{nr}}$ is more than three orders of magnitude (10^3) higher than the $\overline{\Gamma_r}$ for both diabolo nanoantenna and bowtie nanocavity under both polarizations of the nanoemitter. These results confirm the initial assumption that radiation is negligible.

Finally, to quantitatively study the performance of the nanostructures when moving the nanoemitter along the x' axis (Figure 5), the analytical and numerical results of the $\overline{\Gamma_{nr}}$ for both bowtie nanocavity and diabolo nanoantenna for three postions of the nanoemitter ($x' = 0.8$ nm, $x' = 3.6$ nm and $x' = 9.6$ nm) are shown in Figure 6a,b and Figure 6c,d, respectively, when they are illuminated under vertical (first column) and horizontal (second column) polarization of the emitter. Good agreement is obtained between both analytical and numerical results. Let us first evaluate the performance of the fundamental LSP mode of order $n = 1$. For the bowtie nanocavity under vertical polarization (Figure 6a), the $\overline{\Gamma_{nr}}$ has a value of 2.3×10^5 when the nanoemitter is near the center ($x' = 0.8$ nm), it is reduced to 9.6×10^3 at $x' = 0.8$ nm and then it

is increased to 1.7×10^4 at $x' = 9.6$ nm because of the exterior metallic ring, as discussed before). In contrast, for the diabolo nanoantenna (Figure 6c), the $\overline{\Gamma_{nr}}$ at the fundamental LSP mode has a value of 9.02×10^5, 7×10^3 and 1.09×10^3 when the nanoemitter is at $x' = 0.8$ nm, $x' = 3.6$ nm and $x' = 9.6$ nm, respectively, demonstrating that the $\overline{\Gamma_{nr}}$ always decreases when moving the nanoemitter away from the center of the nanoantenna along the x' axis. Under horizontal polarization of the nanoemitter, the $\overline{\Gamma_{nr}}$ for the bowtie nanocavity (Figure 6b) has a value of 6.7×10^3, 3.1×10^3 and 1.4×10^3 when the nanoemitter is at $x' = 0.8$ nm, $x' = 3.6$ nm and $x' = 9.6$ nm, respectively. For the nanoantenna (Figure 6d), the $\overline{\Gamma_{nr}}$ again decreases when moving the nanoemitter far away from the nanoantenna's center with values of 7.2×10^4, 9.6×10^2 and 2.7×10^1 for the same positions along the x' axis, respectively.

From the results shown in Figure 6, it is also interesting to observe how the $\overline{\Gamma_{nr}}$ for the higher order LSP modes increases for the bowtie nanocavity when the nanoemitter is near the outer metallic ring while it always decreases for the diabolo nanoantenna. For instance, for the bowtie nanocavity the LSP mode of order $n = 2$ under vertical polarization of the nanoemitter (Figure 6a) has a value of $\overline{\Gamma_{nr}}$ of 8.6×10^2, 4.8×10^2 and 9.2×10^3 at $x' = 0.8$ nm, $x' = 3.6$ nm and $x' = 9.6$ nm, respectively. On the other hand, the values of $\overline{\Gamma_{nr}}$ for the diabolo nanoantenna are 1.5×10^4, 1.7×10^2 and 3.2×10^1, at the same positions of the nanoemitter along the x' axis, respectively. The same trend is observed for the horizontal polarization. These results are as expected due to the fact that higher number of LSP modes are supported by the bowtie nanocavity compared to the diabolo nanoantenna (as described before in Figure 4). Hence, their $\overline{\Gamma_r}$ will be increased near the exterior metal-air interface.

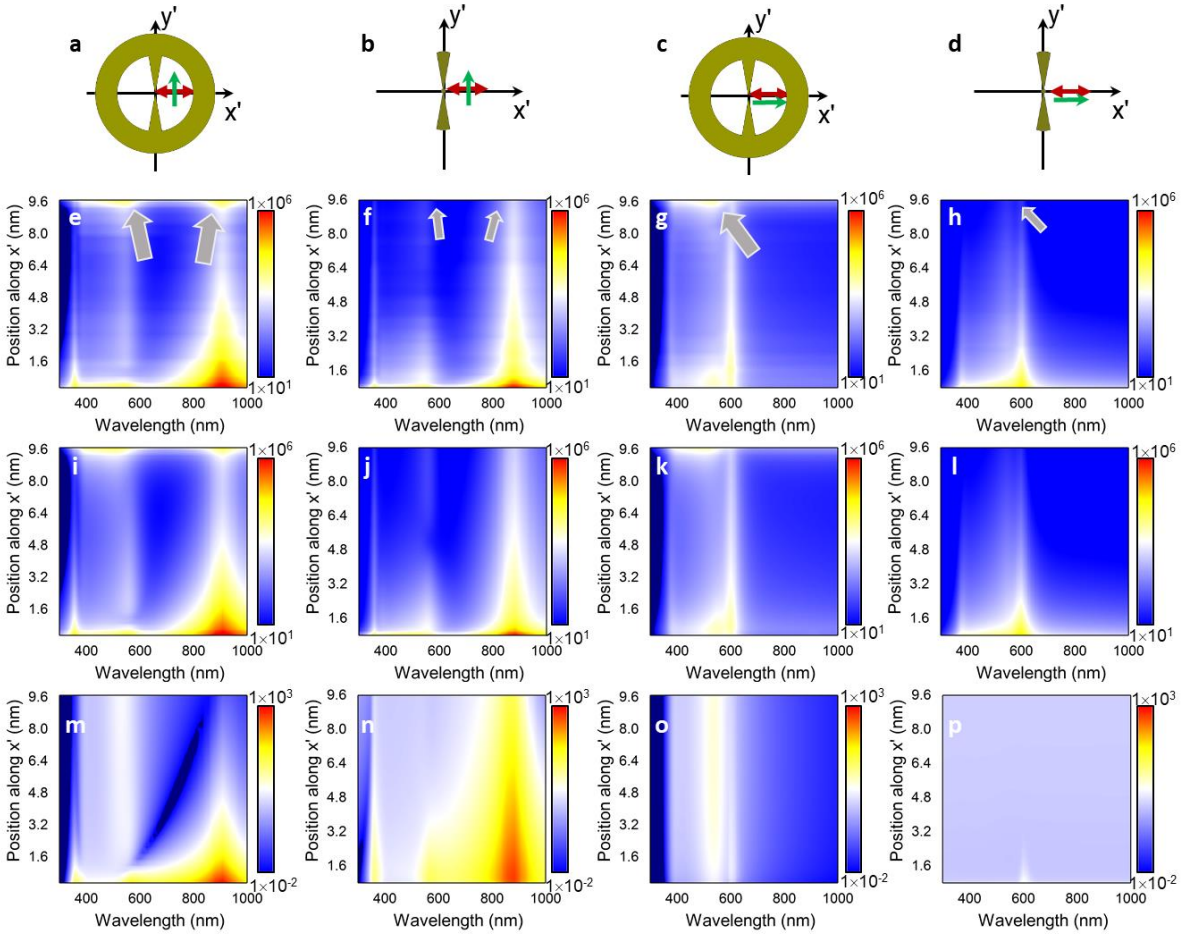

Figure 5. Schematic representation of the bowtie nanocavity (a,c) and diabolo nanoantenna (b,d) under vertical (a,b) and horizontal (c,d) polarization of the nanoemitter. The green arrows represent the nanoemitter, whereas the red arrows indicate the direction along which the dipole is moved. Analytical (second row) and numerical (third row) results of the $\overline{\Gamma_{nr}}$ for the bowtie nanocavity (first and third columns) and diabolo nanoantenna (second and fourth columns) with $\theta' = 20°$ and a vertical (first and second columns) and horizontal (third and four columns) polarization of the nanoemitter when it is located at $y' = 0$ nm and moved along the x' axis. (m-p) Numerical results of the $\overline{\Gamma_r}$ for the bowtie nanocavity (m,o) and diabolo nanoantenna (n,p) under vertical (j,k) and horizontal (l,m) polarization of the nanoemitter.

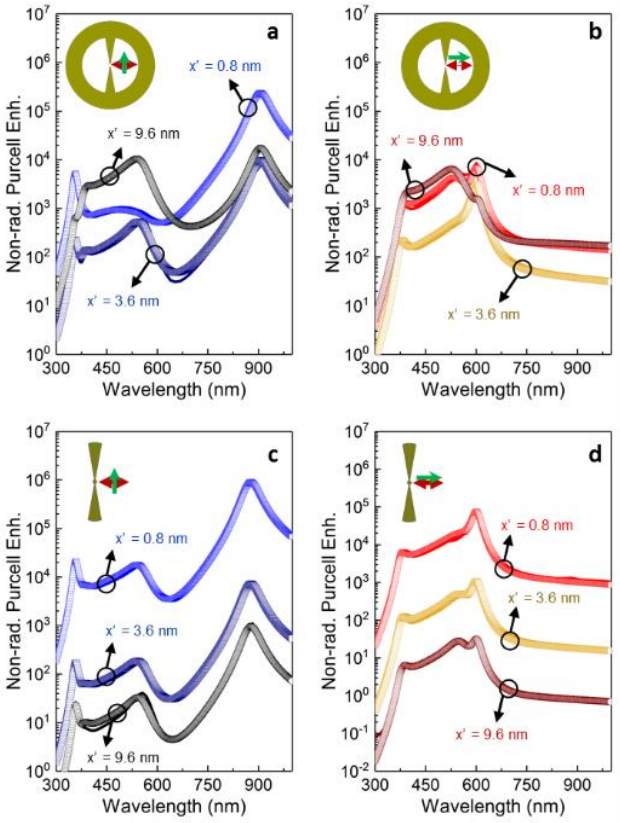

Figure 6. Analytical (symbols) and numerical (solid lines) results of the $\overline{\Gamma_{nr}}$ for a bowtie nanocavity (a,b) and diabolo nanoantenna (c,d) with $\theta' = 20°$ illuminated with a nanoemitter with vertical (a,c) and horizontal (b,d) polarization placed at $y' = 0$ nm and $x' = 0.8$ nm (light blue and light red), $x' = 3.6$ nm (dark blue and yellow) and $x' = 9.6$ nm (black and dark red).

CONCLUSIONS

Counterintuitively, the Purcell enhancement of a nanoemitter in the vicinity of a plasmonic nanostructure does not change if such nanostructure is a diabolo nanoantenna or bowtie nanocavity. This symmetric response for complementary nanostructures cannot be explained in terms of Babinet's principle and full-wave simulations are not of any help to understand the underlying physics. Such symmetric response has been explained unequivocally here resorting to conformal transformation, whereby the hidden symmetry responsible for the identical Purcell enhancement has been unveiled in the suitable coordinate system. The manuscript has also shown that such hidden symmetry governs to certain extend the optical forces experienced by the nanoemitter. Hence, the manuscript illustrates the need of analytical

methods like conformal transformation to make progress in the understanding of plasmonics and its applications.

METHODS

Analytical solutions multislab geometries

Here, the multislab geometries shown in Figure 2 are solved. Due to the fact that the diameter of the diabolo nanoantenna and bowtie nanocavity is considerably smaller than the illuminating wavelength ($l' << \lambda_0$) the near field approximation can be applied. Within this context, the magnetic and electric fields are decoupled and the latter can be described by an electrostatic potential satisfying Laplace's equation. Given that $L_1 + L_2 >> \theta'$, as depicted in the multislab geometries from Figure 2, the primary LSP modes excited in the comb are those propagating along the *x*-axis [46,54]. After applying the conformal mapping, the classical line dipole illuminating the nanostructures in Figure 2a,c is transformed to an array of line dipoles with periodicity of 2π in the multislab scenario with amplitudes depending on the classical line dipole *z'*-position. In the transformed space, the amplitude of the dipoles as a function of the classical line dipole *z'*-position is $\bar{p} = \overline{p'}\frac{1}{a}$, with a as the distance from the dipole to the center of the diabolo nanoantenna and bowtie nanocavity [27]. These considerations are taken into account for the analytical evaluation of the multislab geometries shown in Figure 2. The derivations are shown in the following sub-sections.

Multislab geometry mimicking the gap bowtie nanocavity

Here the analytical formulation for the geometry shown in Figure 2a,b is derived. The electrostatic potentials outside and inside of the metallic slabs in Figure 2b can be calculated as a sum of all the discrete transverse modes, as follows:

$$\sum_k \left[\frac{1}{1+e^{2ik(L_1+L_2)+i\Delta\varphi_1+i\Delta\varphi_2}}\left(e^{ikx}-e^{-ikx+2ikL_1+i\Delta\varphi_1}\right)\times\left(A_+e^{-ky}+B_+e^{-ky}+B_-e^{ky}\right)\right],\quad 0<y<d_1 \tag{1}$$

$$\sum_k \left[\frac{1}{1+e^{2ik(L_1+L_2)+i\Delta\varphi_1+i\Delta\varphi_2}}\left(e^{ikx}-e^{-ikx+2ikL_1+i\Delta\varphi_1}\right)\times\left(A_-e^{ky}+B_+e^{-ky}+B_-e^{ky}\right)\right],\quad -d_2<y<0 \tag{2}$$

$$\sum_k \left[\frac{1}{1+e^{2ik(L_1+L_2)+i\Delta\varphi_1+i\Delta\varphi_2}}\left(e^{ikx}-e^{-ikx+2ikL_1+i\Delta\varphi_1}\right)\times\left(E_+e^{-ky}+E_-e^{ky}\right)\right],\quad -(d_1+2d_2+d_3)<y<-(d_2+d_3) \tag{3}$$

$$\sum_k \left[\frac{1}{1+e^{2ik(L_1+L_2)+i\Delta\varphi_1+i\Delta\varphi_2}}\left(e^{ikx}-e^{-ikx+2ikL_1+i\Delta\varphi_1}\right)\times\left(C_+e^{-ky}+C_-e^{ky}\right)\right],\quad -(d_1+2d_2+2d_3)<y<-(d_1+2d_2+d_3) \tag{4}$$

$$\sum_k \left[\frac{1}{1+e^{2ik(L_1+L_2)+i\Delta\varphi_1+i\Delta\varphi_2}}\left(e^{ikx}-e^{-ikx+2ikL_1+i\Delta\varphi_1}\right)\times\left(D_+e^{-ky}+D_-e^{ky}\right)\right],\quad -(d_2+d_3)<y<-d_2 \tag{5}$$

where k is the wavenumber of the transverse LSP modes; the pairs (B+, B-) and (E+, E-) are the coefficients defining the scattering potential in the region where the dipole is present ($d_2 < y < d_1$) and absent ($d_2 + d_1$), respectively; C+, C-, D+ and D- are the coefficients associated to the potential inside the metallic slabs (d_3), $\Delta\phi_1$ and $\Delta\phi_2$ are the phase corrections applied to take into account the non-perfect reflections that the surface plasmons experience at the right metallic wall and left air region (which are not trivial and depend on both θ' and frequency [59], respectively; A+ and A- are the expansion coefficients of the incident potential which can be

calculated by expanding the potential of the dipole nanoemitter along the *x*-axis via a Fourier transform:

$$A_{\pm} = \frac{\pm p_y - i p_x sgn(k)}{2\varepsilon_0} \tag{6}$$

where ε_0 is the permittivity in free space and p_x and p_y are the two components of the dipole moment along the *x*- and *y*-axis, respectively. Finally, the wavenumber *k* can be calculated as follows:

$$k = \frac{(n\pi - 0.5\Delta\varphi_1 - 0.5\Delta\varphi_2)}{L_1 + L_2} \tag{7}$$

The procedure to calculate the constants B±, C±, D± and E± has been used to analyze other types of nanostructures such as bowtie and tripod nanoantennas and nanocavities [27,28,54] and it is presented here for completeness. The mathematical expressions defining these constants can be calculated by applying boundary conditions at each metal/dielectric interfaces: I) the continuity of the tangential component of the electric field (E_x) at the boundaries $d_2 + d_3$, d_2, d_1 and $d_1 + 2d_2 + 2d_3$ and II) the continuity of the normal component of the displacement current $D_\perp = D_y = \varepsilon_{Au} E_y$ at the same boundaries, as follows:

$$\begin{aligned} &E_+ e^{k(d_2+d_3)} + E_- e^{-k(d_2+d_3)} \\ &-D_+ e^{k(d_2+d_3)} - D_- e^{-k(d_2+d_3)} = 0 \end{aligned} \tag{8}$$

$$\begin{aligned} &E_+ e^{k(d_2+d_3)} - E_- e^{-k(d_2+d_3)} \\ &-\varepsilon_{Au} D_+ e^{k(d_2+d_3)} + \varepsilon_{Au} D_- e^{-k(d_2+d_3)} = 0 \end{aligned} \tag{9}$$

$$\begin{aligned} &A_- e^{-kd_2} + B_+ e^{kd_2} + B_- e^{-kd_2} \\ &-D_+ e^{kd_2} - D_- e^{-kd_2} = 0 \end{aligned} \tag{10}$$

$$\begin{aligned} &A_- e^{-kd_2} - B_+ e^{kd_2} + B_- e^{-kd_2} \\ &+\varepsilon_{Au} D_+ e^{kd_2} - D\varepsilon_{Au\_} e^{-kd_2} = 0 \end{aligned} \tag{11}$$

$$A_+e^{-kd_1} + B_+e^{-kd_1} + B_-e^{kd_1} - C_+e^{k(d_1+2d_2+2d_3)} - C_-e^{-k(d_1+2d_2+2d_3)} = 0 \quad (12)$$

$$A_+e^{-kd_1} + B_+e^{-kd_1} - B_-e^{kd_1} - \varepsilon_{Au}C_+e^{k(d_1+2d_2+2d_3)} + \varepsilon_{Au}C_-e^{-k(d_1+2d_2+2d_3)} = 0 \quad (13)$$

$$E_+e^{k(d_1+2d_2+d_3)} + E_-e^{-k(d_1+2d_2+d_3)} - C_+e^{k(d_1+2d_2+d_3)} - C_-e^{-k(d_1+2d_2+d_3)} = 0 \quad (14)$$

$$-E_+e^{k(d_1+2d_2+d_3)} + E_-e^{-k(d_1+2d_2+d_3)} + \varepsilon_{Au}C_+e^{k(d_1+2d_2+d_3)} - \varepsilon_{Au}C_-e^{-k(d_1+2d_2+d_3)} = 0 \quad (15)$$

where ε_{Au} is the permittivity of the plasmonic metal used in this work (gold). The solution of each constant is not shown here for the sake of brevity. However, they can be straightforwardly calculated either manually or with a mathematical software. The resonant condition and the cut-off wavelength for the LSP modes shown in Figure 4 can be calculated taking into account the divergence of the coefficient of the scattered potential in the region where the dipole is present (B±) and corresponds to that shown in [28].

Once all the coefficients have been defined, the solutions of the potential where the dipole is and is not present (ϕ_1^S and ϕ_2^S, respectively) can be calculated by using an inverse transform to the induced potentials:

$$\phi_1^{S1} = \Omega \sum_n \{p_x[\sin(kx) + \sin(kx - 2kL_1 - \Delta\varphi_1)] + p_y[\cos(kx) - \cos(kx - 2kL_1 - \Delta\varphi_1)]\} \times (B_+e^{-ky} + B_-e^{ky})] \quad (16)$$

$$\phi_2^{S1} = \Omega \sum_n \{p_x[\sin(kx) + \sin(kx - 2kL_1 - \Delta\varphi_1)] + p_y[\cos(kx) - \cos(kx - 2kL_1 - \Delta\varphi_1)]\} \times (E_+ e^{-ky} + E_- e^{ky})] \quad (17)$$

with $\Omega = 1/2\varepsilon_0(L_1 + L_2)$. Following the same procedure, the expressions defining the potentials for the top and bottom arms of the Bow-tie nanocavity (ϕ_1^{m1} and ϕ_2^{m1}, respectively) can be calculated as follows:

$$\phi_1^{m1} = \Omega \sum_n \{p_x[\sin(kx) + \sin(kx - 2kL_1 - \Delta\varphi_1)] + p_y[\cos(kx) - \cos(kx - 2kL_1 - \Delta\varphi_1)]\} \times (C_+ e^{-ky} + C_- e^{ky})] \quad (18)$$

$$\phi_2^{m} = \Omega \sum_n \{p_x[\sin(kx) + \sin(kx - 2kL_1 - \Delta\varphi_1)] + p_y[\cos(kx) - \cos(kx - 2kL_1 - \Delta\varphi_1)]\} \times (D_+ e^{-ky} + D_- e^{ky})] \quad (19)$$

The analytical expressions for the components of the electric field along the *x*- and *y*- axes outside and inside the metallic slabs can be obtained by simply differentiating the potentials from Equation 16-19, as follows:

$$E_{1x}^{S1} = -k\Omega \sum_n \{p_x[\cos(kx) + \cos(kx - 2kL_1 - \Delta\varphi_1)] - p_y[\sin(kx) - \sin(kx - 2kL_1 - \Delta\varphi_1)]\} \times (B_+ e^{-ky} + B_- e^{ky})] \quad (20)$$

$$E_{2x}^{S1} = -k\Omega \sum_n \{p_x[\cos(kx) + \cos(kx - 2kL_1 - \Delta\varphi_1)] - p_y[\sin(kx) - \sin(kx - 2kL_1 - \Delta\varphi_1)]\} \times (E_+ e^{-ky} + E_- e^{ky})] \quad (21)$$

$$E_{1x}^{m1} = -k\Omega \sum_n \{p_x[\cos(kx) + \cos(kx - 2kL_1 - \Delta\varphi_1)] - p_y[\sin(kx) - \sin(kx - 2kL_1 - \Delta\varphi_1)]\} \times (C_+ e^{-ky} + C_- e^{ky})] \quad (22)$$

$$E_{2x}^{m1} = -k\Omega \sum_n \{p_x[\cos(kx) + \cos(kx - 2kL_1 - \Delta\varphi_1)] - p_y[\sin(kx) - \sin(kx - 2kL_1 - \Delta\varphi_1)]\} \times (D_+ e^{-ky} + D_- e^{ky})] \quad (23)$$

$$E_{1y}^{S1} = -k\Omega \sum_n \{p_x[\sin(kx) + \sin(kx - 2kL_1 - \Delta\varphi_1)] + p_y[\cos(kx) - \cos(kx - 2kL_1 - \Delta\varphi_1)]\} \times (-B_+ e^{-ky} + B_- e^{ky})] \quad (24)$$

$$E_{2y}^{S1} = -k\Omega \sum_n \{p_x[\sin(kx) + \sin(kx - 2kL_1 - \Delta\varphi_1)] + p_y[\cos(kx) - \cos(kx - 2kL_1 - \Delta\varphi_1)]\} \times (-E_+ e^{-ky} + E_- e^{ky})] \quad (25)$$

$$E_{1y}^{m1} = -k\Omega \sum_n \{p_x[\sin(kx) + \sin(kx - 2kL_1 - \Delta\varphi_1)] + p_y[\cos(kx) - \cos(kx - 2kL_1 - \Delta\varphi_1)]\} \times (-C_+ e^{-ky} + C_- e^{ky})] \quad (26)$$

$$E_{2y}^{m1} = -k\Omega \sum_n \{p_x[\sin(kx) + \sin(kx - 2kL_1 - \Delta\varphi_1)] + p_y[\cos(kx) - \cos(kx - 2kL_1 - \Delta\varphi_1)]\} \times (-D_+ e^{-ky} + D_- e^{ky})] \quad (27)$$

Multislab geometry mimicking the connected diabolo nanoantenna

Here the analytical formulation for the geometry shown in Figure 2c,d is derived following the same procedure shown in the previous section. The electrostatic potentials outside and inside of the metallic slabs in Figure 2d can be defined as follows:

$$\sum_k \left[\frac{1}{1+e^{2ik(L_1+L_2)+i\Delta\varphi_1+i\Delta\varphi_2}}\left(e^{ikx}+e^{-ikx+2ikL_1+i\Delta\varphi_1}\right)\right.$$
$$\left.\times\left(A_+e^{-ky}+B_+e^{-ky}+B_-e^{ky}\right)\right], \quad 0<y<d_1 \tag{28}$$

$$\sum_k \left[\frac{1}{1+e^{2ik(L_1+L_2)+i\Delta\varphi_1+i\Delta\varphi_2}}\left(e^{ikx}+e^{-ikx+2ikL_1+i\Delta\varphi_1}\right)\right.$$
$$\left.\times\left(A_-e^{ky}+B_+e^{-ky}+B_-e^{ky}\right)\right], \quad -d_2<y<0 \tag{29}$$

$$\sum_k \left[\frac{1}{1+e^{2ik(L_1+L_2)+i\Delta\varphi_1+i\Delta\varphi_2}}\left(e^{ikx}+e^{-ikx+2ikL_1+i\Delta\varphi_1}\right)\right.$$
$$\left.\times\left(E_+e^{-ky}+E_-e^{ky}\right)\right], \quad -(d_1+2d_2+d_3)<y<-(d_2+d_3) \tag{30}$$

$$\sum_k \left[\frac{1}{1+e^{2ik(L_1+L_2)+i\Delta\varphi_1+i\Delta\varphi_2}}\left(e^{ikx}+e^{-ikx+2ikL_1+i\Delta\varphi_1}\right)\right.$$
$$\left.\times\left(C_+e^{-ky}+C_-e^{ky}\right)\right], \quad -(d_1+2d_2+2d_3)<y<-(d_1+2d_2+d_3) \tag{31}$$

$$\sum_k \left[\frac{1}{1+e^{2ik(L_1+L_2)+i\Delta\varphi_1+i\Delta\varphi_2}}\left(e^{ikx}+e^{-ikx+2ikL_1+i\Delta\varphi_1}\right)\right.$$
$$\left.\times\left(D_+e^{-ky}+D_-e^{ky}\right)\right], \quad -(d_2+d_3)<y<-d_2 \tag{32}$$

where the A± , B±, C±, D± and E± are those calculated in the previous section for the gap bowtie nanocavity. The solutions of the potential where the dipole is and is not present (ϕ_1^{S2} and ϕ_2^{S2}, respectively) and the potentials for the top and bottom arms of the diabolo nanoantenna (ϕ_1^{m2} and ϕ_2^{m2}) can be calculated by using an inverse transform to the induced potentials:

$$\phi_1^{S2} = \Omega\sum_n\{p_x[\sin(kx)-\sin(kx-2kL_1-\Delta\varphi_1)] + p_y[\cos(kx)+\cos(kx-2kL_1-\Delta\varphi_1)]\} \times\left(B_+e^{-ky}+B_-e^{ky}\right)] \tag{33}$$

$$\phi_2^{S2} = \Omega \sum_n \{p_x[\sin(kx) - \sin(kx - 2kL_1 - \Delta\varphi_1)] + p_y[\cos(kx) + \cos(kx - 2kL_1 - \Delta\varphi_1)]\} \times (E_+ e^{-ky} + E_- e^{ky})] \quad (34)$$

$$\phi_1^{m2} = \Omega \sum_n \{p_x[\sin(kx) - \sin(kx - 2kL_1 - \Delta\varphi_1)] + p_y[\cos(kx) + \cos(kx - 2kL_1 - \Delta\varphi_1)]\} \times (C_+ e^{-ky} + C_- e^{ky})] \quad (35)$$

$$\phi_2^{m2} = \Omega \sum_n \{p_x[\sin(kx) - \sin(kx - 2kL_1 - \Delta\varphi_1)] + p_y[\cos(kx) + \cos(kx - 2kL_1 - \Delta\varphi_1)]\} \times (D_+ e^{-ky} + D_- e^{ky})] \quad (36)$$

Finally, after differentiating the potentials from Equation 33-36, the *x*- and *y*- components of the electric field outside and inside the metallic slabs are as follows:

$$E_{1x}^{S2} = -k\Omega \sum_n \{p_x[\cos(kx) - \cos(kx - 2kL_1 - \Delta\varphi_1)] - p_y[\sin(kx) + \sin(kx - 2kL_1 - \Delta\varphi_1)]\} \times (B_+ e^{-ky} + B_- e^{ky})] \quad (37)$$

$$E_{2x}^{S2} = -k\Omega \sum_n \{p_x[\cos(kx) - \cos(kx - 2kL_1 - \Delta\varphi_1)] - p_y[\sin(kx) + \sin(kx - 2kL_1 - \Delta\varphi_1)]\} \times (E_+ e^{-ky} + E_- e^{ky})] \quad (38)$$

$$E_{1x}^{m2} = -k\Omega \sum_n \{p_x[\cos(kx) - \cos(kx - 2kL_1 - \Delta\varphi_1)] - p_y[\sin(kx) + \sin(kx - 2kL_1 - \Delta\varphi_1)]\} \times (C_+ e^{-ky} + C_- e^{ky})] \quad (39)$$

$$E_{2x}^{m2} = -k\Omega \sum_n \{p_x[\cos(kx) - \cos(kx - 2kL_1 - \Delta\varphi_1)] - p_y[\sin(kx) + \sin(kx - 2kL_1 - \Delta\varphi_1)]\} \times (D_+ e^{-ky} + D_- e^{ky})] \quad (40)$$

$$E_{1y}^{S2} = -k\Omega \sum_n \{p_x[\sin(kx) - \sin(kx - 2kL_1 - \Delta\varphi_1)] + p_y[\cos(kx) + \cos(kx - 2kL_1 - \Delta\varphi_1)]\} \times (-B_+ e^{-ky} + B_- e^{ky})] \quad (41)$$

$$E_{2y}^{S2} = -k\Omega \sum_n \{p_x[\sin(kx) - \sin(kx - 2kL_1 - \Delta\varphi_1)] + p_y[\cos(kx) + \cos(kx - 2kL_1 - \Delta\varphi_1)]\} \times (-E_+ e^{-ky} + E_- e^{ky})] \quad (42)$$

$$E_{1y}^{m2} = -k\Omega \sum_n \{p_x[\sin(kx) - \sin(kx - 2kL_1 - \Delta\varphi_1)] + p_y[\cos(kx) + \cos(kx - 2kL_1 - \Delta\varphi_1)]\} \times (-C_+ e^{-ky} + C_- e^{ky})] \quad (43)$$

$$E_{2y}^{m2} = -k\Omega \sum_n \{p_x[\sin(kx) - \sin(kx - 2kL_1 - \Delta\varphi_1)] + p_y[\cos(kx) + \cos(kx - 2kL_1 - \Delta\varphi_1)]\} \times (-D_+ e^{-ky} + D_- e^{ky})] \quad (44)$$

Phase corrections under vertical and horizontal polarizations of the nanoemitter

The procedure to obtain the values of $\Delta\phi_1$ and $\Delta\phi_2$ is performed by fitting the analytically calculated wavelength of the fundamental LSP mode ($n = 1$) to the numerical results, as follows:

For the gap bowtie nanocavity shown in Figure 2a,b, the bowtie nanocavity without a gap (diabolo nanocavity) [28] is studied first. Due to the fact that such nanocavity has metal walls at both edges, it is only needed to estimate one phase correction (namely $\Delta\phi$). It is extracted by fitting the analytical to the numerical wavelength of the bowtie nanocavity. Then, this $\Delta\phi$ is used as $\Delta\phi_1$ for the gap bowtie nanocavity from Figure 2a,b since it corresponds to the complex reflection at the metal edge [right hand side of the multislab geometry from Figure 2b]. Once this is done, the only unknown left is $\Delta\phi_2$ (which accounts for the complex reflection at the gap between the two arms of the gap bowtie nanocavity [left edge from the multislab geometry of

Figure 2b]. This $\Delta\phi_2$ is then estimated by fitting the analytical to the numerically-computed wavelength of the gap bowtie nanocavity fundamental LSP mode. The values of $\Delta\phi_1$ and $\Delta\phi_2$ as a function of the angular aperture of the arms (θ') for both vertical and horizontal polarization of nanoemitter are shown in Figure 7a,b and Figure 7c,d, respectively, and can be mathematically described as follows:

$$\Delta\varphi_1(\theta')_v = 0.36 - \frac{0.61}{\left\{1+e^{\left[16.05\left(\theta'-0.66\right)\right]}\right\}} \tag{45}$$

$$\Delta\varphi_2(\theta')_v = 0.96 - \frac{0.081}{\left\{1+e^{\left[7.9\left(\theta'-18.81\right)\right]}\right\}} \tag{46}$$

$$\Delta\varphi_1(\theta')_h = 2.05 - \frac{0.13}{\left\{1+e^{\left[5\left(\theta'-24.04\right)\right]}\right\}} \tag{47}$$

$$\Delta\varphi_2(\theta')_h = 0.83 - \frac{0.27}{\left\{1+e^{\left[7.6\left(\theta'-23.48\right)\right]}\right\}} \tag{48}$$

A similar process is used to calculate the values of $\Delta\phi_1$ and $\Delta\phi_2$ for the connected diabolo nanoantenna shown in Figure 2c,d. For this structure, the gap bowtie nanoantenna [54] is studied first.

Since such nanoantenna has no metallic walls at the edges (open-ended), it is only required to obtain again one phase correction, $\Delta\phi$. It is extracted by fitting the analytical to the numerical wavelength of the gap bowtie nanoantenna. Then, this $\Delta\phi = \Delta\phi_1$ for the connected diabolo nanoantenna from Figure 2c since it corresponds to the complex reflection at the open-ended edge [right hand side of the multislab geometry from Figure 2d]. Finally, the unknown $\Delta\phi_2$ [corresponding to the complex reflection at the left edge from the multislab geometry of Figure 2d]. This $\Delta\phi_2$ is then estimated by fitting the analytical to the numerically-computed wavelength of the connected diabolo nanoantenna fundamental LSP mode. The values of $\Delta\phi_1$ and $\Delta\phi_2$ as a function of the angular aperture of the arms (θ') for both vertical and horizontal polarization of nanoemitter for the connected diabolo nanoantenna are shown in Figure 7e,f and Figure 7g,h, respectively, and can be mathematically defined as follows:

$$\Delta\varphi_1(\theta')_v = 0.29 - \frac{2.07}{\left\{1+e^{\left[37\left(\theta'+108.16\right)\right]}\right\}} \tag{49}$$

$$\Delta\varphi_2(\theta')_v = 1.07 - \frac{0.05}{\left\{1+e^{\left[3.03\left(\theta'-20.24\right)\right]}\right\}} \tag{50}$$

$$\Delta\varphi_1(\theta')_h = 0.28 - \frac{0.06}{\left\{1+e^{\left[2.1\left(\theta'-20.76\right)\right]}\right\}} \tag{51}$$

$$\Delta\varphi_2(\theta')_h = 0.97 - \frac{0.045}{\left\{1+e^{\left[1.4\left(\theta'-18.7\right)\right]}\right\}} \tag{52}$$

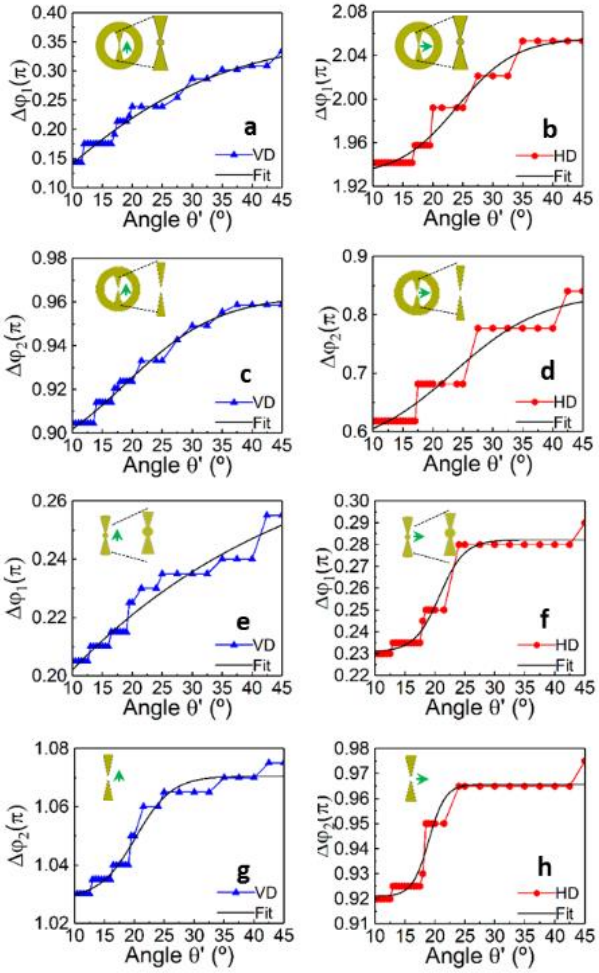

Figure 7. Phase correction $\Delta\phi_1$ (first and third rows) and $\Delta\phi_2$ (second and third rows) as a function of θ' for bowtie nanocavities (first and second rows) and diabolo nanoantennas (third and fourth rows) under vertical (first column) and horizontal (second column) polarization of the nanoemitter.

ASSOCIATED CONTENT

Supporting information

The Supporting Information is available free of charge on the ACS Publications website at DOI:

Results of the $\overline{\Gamma_{nr}}$ for bowtie nanocavities (first row), diabolo nanoantennas (second row) and diabolo nanocavities (third row) under vertical polarization of the nanoemitter (Figure S1).

Numerical results of the $\overline{\Gamma_{nr}}$ for 3D bowtie nanocavities and diabolo nanoantennas (Figure S2).

$\overline{\Gamma_{nr}}$ for diabolo nanoantennas and bowtie nanocavities with complementary geometries (Figure S3).

AUTHOR INFORMATION

Corresponding Authors

* School of Engineering, Newcastle University, Merz Court, Newcastle Upon Tyne NE1 7RU, UK.

* School of Physics and Astronomy, University of Birmingham, Birmingham B15 2TT, UK. m.navarro-cia@bham.ac.uk; Phone: +44(0)1214144664; Fax: +44(0)1214144644

ACKNOWLEDGEMENTS

V. P-P. is supported by the Newcastle University (Newcastle University Research Fellow). R. A. is supported by the University of Birmingham (PhD studentship). M. N.-C. is supported by the University of Birmingham (Birmingham Fellowship).

REFERENCES

(1) Schuller, J. A.; Barnard, E. S.; Cai, W.; Jun, Y. C.; White, J. S.; Brongersma, M. L. Plasmonics for Extreme Light Concentration and Manipulation. *Nat. Mater.* **2010**, *9* (3), 193–204. https://doi.org/10.1038/nmat2630.

(2) Neumann, T.; Johansson, M.-L.; Kambhampati, D.; Knoll, W. Surface-Plasmon Fluorescence Spectroscopy. *Adv. Funct. Mater.* **2002**, *12* (9), 575–586. https://doi.org/10.1002/1616-3028(20020916)12:9<575::AID-ADFM575>3.0.CO;2-4.

(3) Pacheco-Peña, V.; Minin, I. V; Minin, O. V; Beruete, M. Increasing Surface Plasmons Propagation via Photonic Nanojets with Periodically Spaced 3D Dielectric Cuboids. *Photonics* **2016**, *3* (10), 1–7. https://doi.org/10.3390/www.mdpi.com/journal/photonics.

(4) Chen, C.; Hutchison, J. A.; Van Dorpe, P.; Kox, R.; De Vlaminck, I.; Uji-I, H.; Hofkens, J.; Lagae, L.; Maes, G.; Borghs, G. Focusing Plasmons in Nanoslits for Surface-Enhanced Raman Scattering. *Small* **2009**, *5* (24), 2876–2882. https://doi.org/10.1002/smll.200901312.

(5) Hu, E. L. Applications: Nanophotonics and Plasmonics. In *Nanotechnology Research Directions for Societal Needs in 2020*; Springer, Dordrecht: Dordrecht, 2011; pp 417–444.

(6) Kabashin, A. V.; Evans, P.; Pastkovsky, S.; Hendren, W.; Wurtz, G. A.; Atkinson, R.; Pollard, R.; Podolskiy, V. A.; Zayats, A. V. Plasmonic Nanorod Metamaterials for Biosensing. *Nat. Mater.* **2009**, *8* (11), 867–871. https://doi.org/10.1038/nmat2546.

(7) Coyle, S.; Netti, M. C.; Baumberg, J. J.; Ghanem, M. A.; Birkin, P. R.; Bartlett, P. N.; Whittaker, D. M. Confined Plasmons in Metallic Nanocavities. *Adv. Mater.* **2001**, *87* (17), 1368–1370. https://doi.org/10.1103/PhysRevLett.87.176801.

(8) S. A. Maier. *Plasmonics: Fundamentals and Applications*, First Edit.; Springer, 2007.

(9) Chikkaraddy, R.; Nijs, B. De; Benz, F.; Barrow, S. J.; Scherman, O. A.; Rosta, E.; Demetriadou, A.; Fox, P.; Hess, O.; Baumberg, J. J. Single-Molecule Strong Coupling

at Room Temperature in Plasmonic Nanocavities. *Nature* **2016**, *535* (127), 1–4. https://doi.org/10.1038/nature17974.

(10) Giordano, M. C.; Longhi, S.; Barelli, M.; Mazzanti, A.; Buatier de Mongeot, F.; Della Valle, G. Plasmon Hybridization Engineering in Self-Organized Anisotropic Metasurfaces. *Nano Res.* **2018**, *11* (7), 3943–3956. https://doi.org/10.1007/s12274-018-1974-3.

(11) Rajeeva, B. B.; Lin, L.; Zheng, Y. Design and Applications of Lattice Plasmon Resonances. *Nano Res.* **2018**, *11* (9), 4423–4440. https://doi.org/10.1007/s12274-017-1909-4.

(12) Liu, Z.; Steele, J. M.; Srituravanich, W.; Pikus, Y.; Sun, C.; Zhang, X. Focusing Surface Plasmons with a Plasmonic Lens. *Nano Lett.* **2005**, *5* (9), 1726–1729. https://doi.org/10.1021/nl051013j.

(13) Wang, W.; Gu, J.; He, T.; Shen, Y.; Xi, S.; Tian, L.; Li, F.; Li, H.; Yan, L.; Zhou, X. Optical Super-Resolution Microscopy and Its Applications in Nano-Catalysis. *Nano Res.* **2015**, *8* (2), 441–455. https://doi.org/10.1007/s12274-015-0709-y.

(14) Fang, N.; Lee, H.; Sun, C.; Zhang, X. Sub-Diffraction-Limited Optical Imaging with a Silver Superlens. *Science* **2005**, *308* (5721), 534–537. https://doi.org/10.1126/science.1108759.

(15) Shoji, T.; Tsuboi, Y. Plasmonic Optical Tweezers toward Molecular Manipulation: Tailoring Plasmonic Nanostructure, Light Source, and Resonant Trapping. *J. Phys. Chem. Lett.* **2014**, *5*, 2957–2967.

(16) Righini, M.; Ghenuche, P.; Cherukulappurath, S.; Myroshnychenko, V.; De García Abajo, F. J.; Quidant, R. Nano-Optical Trapping of Rayleigh Particles and Escherichia Coli Bacteria with Resonant Optical Antennas. *Nano Lett.* **2009**, *9* (10), 3387–3391. https://doi.org/10.1021/nl803677x.

(17) Roxworthy, B. J.; Toussaint, K. C. Femtosecond-Pulsed Plasmonic Nanotweezers. *Sci.*

Rep. **2012**, *2*, 1–6. https://doi.org/10.1038/srep00660.

(18) Navarro-Cía, M.; Maier, S. A. Broad-Band near-Infrared Plasmonic Nanoantennas for Higher Harmonic Generation. *ACS Nano* **2012**, *6* (4), 3537–3544. https://doi.org/10.1021/nn300565x.

(19) Aouani, H.; Rahmani, M.; Navarro-Cía, M.; Maier, S. A. Third-Harmonic-Upconversion Enhancement from a Single Semiconductor Nanoparticle Coupled to a Plasmonic Antenna. *Nat. Nanotechnol.* **2014**, *9* (4), 290–294. https://doi.org/10.1038/nnano.2014.27.

(20) Sivis, M.; Duwe, M.; Abel, B.; Ropers, C. Extreme-Ultraviolet Light Generation in Plasmonic Nanostructures. *Nat. Phys.* **2013**, *9* (4), 304–309. https://doi.org/10.1038/nphys2590.

(21) Afinogenov, B. I.; Popkova, A. A.; Bessonov, V. O.; Lukyanchuk, B.; Fedyanin, A. A. Phase Matching with Tamm Plasmons for Enhanced Second- and Third-Harmonic Generation. *Phys. Rev. B* **2018**, *97* (11), 1–5. https://doi.org/10.1103/PhysRevB.97.115438.

(22) Aouani, H.; Navarro-Cia, M.; Rahmani, M.; Sidiropoulos, T. P. H.; Hong, M.; Oulton, R. F.; Maier, S. A. Multiresonant Broadband Optical Antennas As Efficient Tunable Nanosources of Second Harmonic Light. *Nano Lett.* **2012**, *12*, 4997–5002.

(23) Alù, A.; Engheta, N. Input Impedance, Nanocircuit Loading, and Radiation Tuning of Optical Nanoantennas. *Phys. Rev. Lett.* **2008**, *101* (July), 1–4. https://doi.org/10.1103/PhysRevLett.101.043901.

(24) Straubel, J.; Filter, R.; Rockstuhl, C.; Słowik, K. A Plasmonic Nanoantenna Based Triggered Single Photon Source. *Phys. Rev. B* **2016**, *195412*, 1510.07906. https://doi.org/10.1103/PhysRevB.93.195412.

(25) Chen, P.-Y.; Argyropoulos, C.; Alù, A. Enhanced Nonlinearities Using Plasmonic Nanoantennas. *Nanophotonics* **2012**, *1* (3–4), 221–233. https://doi.org/10.1515/nanoph-

2012-0016.

(26) Chen, S.; Wang, Z. L.; Ballato, J.; Foulger, S. H.; Carroll, D. L. Monopod, Bipod, Tripod, and Tetrapod Gold Nanocrystals. *J. Am. Chem. Soc.* **2003**, *125*, 16186–16187. https://doi.org/10.1021/ja038927x.

(27) Pacheco-Peña, V.; Fernández-Domínguez, A. I.; Luo, Y.; Beruete, M.; Navarro-Cía, M. Aluminum Nanotripods for Light-Matter Coupling Robust to Nanoemitter Orientation. *Laser Photon. Rev.* **2017**, *1700051*, 1700051. https://doi.org/10.1002/lpor.201700051.

(28) Pacheco-Peña, V.; Navarro-Cía, M. Understanding Quantum Emitters in Plasmonic Nanocavities with Conformal Transformation: Purcell Enhancement and Forces. *Nanoscale* **2018**, *10*, 13607–13616. https://doi.org/10.1039/C8NR01527A.

(29) Roxworthy, B. J.; Ko, K. D.; Kumar, A.; Fung, K. H.; Chow, E. K. C.; Liu, G. L.; Fang, N. X.; Toussaint, K. C. Application of Plasmonic Bowtie Nanoantenna Arrays for Optical Trapping, Stacking, and Sorting. *Nano Lett.* **2012**, *12* (2), 796–801. https://doi.org/10.1021/nl203811q.

(30) Kinkhabwala, A.; Yu, Z.; Fan, S.; Avlasevich, Y.; Mullen, K.; E., M. Large Single-Molecule Fluorescence Enhancements Produced by a Bowtie Nanoantenna. *Nat. Photonics* **2009**, *3* (11), 654–657.

(31) Santhosh, K.; Bitton, O.; Chuntonov, L.; Haran, G. Vacuum Rabi Splitting in a Plasmonic Cavity at the Single Quantum Emitter Limit. *Nat. Commun.* **2016**, *7* (11823). https://doi.org/10.1038/ncomms11823.

(32) Rosen, D. A.; Tao, A. R. Modeling the Optical Properties of Bowtie Antenna Generated by Self-Assembled Ag Triangular Nanoprisms. *ACS Appl. Mater. Interfaces* **2014**, *6* (6), 4134–4142. https://doi.org/10.1021/am4057612.

(33) Wang, L.; M. Uppuluri, S.; X. Jin, E.; Xu, X. Nanolithography Using High Transmission Nanoapertures. *Nanoletters* **2006**, *6* (3), 361–364. https://doi.org/10.1117/2.1200604.0214.

(34) Sundaramurthy, A.; Schuck, P. J.; Conley, N. R.; Fromm, D. P.; Kino, G. S.; Moerner, W. E. Toward Nanometer-Scale Optical Photolithography: Utilizing the Near-Field of Bowtie Optical Nanoantennas. *Nano Lett.* **2006**, *6* (3), 355–360. https://doi.org/10.1021/nl052322c.

(35) Mivelle, M.; Van Zanten, T. S.; Neumann, L.; Van Hulst, N. F.; Garcia-Parajo, M. F. Ultrabright Bowtie Nanoaperture Antenna Probes Studied by Single Molecule Fluorescence. *Nano Lett.* **2012**, *12* (11), 5972–5978. https://doi.org/10.1021/nl303440w.

(36) Yong, J.; Bian, H.; Yang, Q.; Lu, Y.; Chen, F.; Hou, X.; Du, G. Tunable Potential Well for Plasmonic Trapping of Metallic Particles by Bowtie Nano-Apertures. *Sci. Rep.* **2016**, *6* (1), 1–8. https://doi.org/10.1038/srep32675.

(37) Balanis, C. A. *Antenna Theory: Analysis and Design*, Third Edit.; John Wiley & Sons: Hoboken, New Jersey, 2005; Vol. 72. https://doi.org/10.1109/PROC.1984.12959.

(38) Giannini, V.; Fernández-Domínguez, A. I.; Heck, S. C.; Maier, S. A. Plasmonic Nanoantennas: Fundamentals and Their Use in Controlling the Radiative Properties of Nanoemitters. *Chem. Rev.* **2011**, *111* (6), 3888–3912. https://doi.org/10.1021/cr1002672.

(39) Gallinet, B.; Butet, J.; Martin, O. J. F. Numerical Methods for Nanophotonics: Standard Problems and Future Challenges. *Laser Photonics Rev.* **2015**, *9* (6), 577–603. https://doi.org/10.1002/lpor.201500122.

(40) Xu, L.; Chen, H. Conformal Transformation Optics. *Nat. Photonics* **2014**, *9* (1), 1–8. https://doi.org/10.1038/nphoton.2014.307.

(41) Pendry, J. B.; Luo, Y.; Zhao, R. Transforming the Optical Landscape. *Science (80-.).* **2015**, *348* (6234), 521–524. https://doi.org/10.1126/science.1261244.

(42) Pendry, J. B.; Aubry, A.; Smith, D. R.; Maier, S. A. Transformation Optics and Subwavelength Control of Light. *Science* **2012**, *337* (6094), 549–552.

https://doi.org/10.1126/science.1220600.

(43) Pendry, J. B.; Fernández-Domínguez, A. I.; Luo, Y.; Zhao, R. Capturing Photons with Transformation Optics. *Nat. Phys.* **2013**, *9*, 518–522.

(44) Luo, Y.; Lei, D. Y.; Maier, S. A.; Pendry, J. B. Transformation-Optics Description of Plasmonic Nanostructures Containing Blunt Edges/Corners: From Symmetric to Asymmetric Edge Rounding. *ACS Nano* **2012**, *6* (7), 6492–6506. https://doi.org/10.1021/nn3022684.

(45) Luo, Y.; Pendry, J. B.; Aubry, A. Surface Plasmons and Singularities. *Nano Lett.* **2010**, *10* (10), 4186–4191. https://doi.org/10.1021/nl102498s.

(46) Luo, Y.; Lei, D. Y.; Maier, S. A.; Pendry, J. B. Broadband Light Harvesting Nanostructures Robust to Edge Bluntness. *Phys. Rev. Lett.* **2012**, *108* (2), 023901. https://doi.org/10.1103/PhysRevLett.108.023901.

(47) Fernández-Domínguez, A. I.; Wiener, A.; García-Vidal, F. J.; Maier, S. A.; Pendry, J. B. Transformation-Optics Description of Nonlocal Effects in Plasmonic Nanostructures. *Phys. Rev. Lett.* **2012**, *108* (10), 1–5. https://doi.org/10.1103/PhysRevLett.108.106802.

(48) Lei, D. Y.; Aubry, A.; Luo, Y.; Maier, S. A.; Pendry, J. B. Plasmonic Interaction between Overlapping Nanowires. *ACS Nano* **2011**, *5* (1), 597–607. https://doi.org/10.1021/nn102819p.

(49) Luo, Y.; Zhao, R. K.; Fernandez-Dominguez, A. I.; Maier, S. A.; Pendry, J. B. Harvesting Light with Transformation Optics. *Sci. China Inf. Sci.* **2013**, *56* (12), 1–13. https://doi.org/10.1007/s11432-013-5031-2.

(50) Fernández-Domínguez, A. I.; Luo, Y.; Wiener, A.; Pendry, J. B.; Maier, S. A. Theory of Three-Dimensional Nanocrescent Light Harvesters. *Nano Lett.* **2012**, *12*, 5946–5953. https://doi.org/10.1021/nl303377g.

(51) Kraft, M.; Pendry, J. B.; Maier, S. A.; Luo, Y. Transformation Optics and Hidden

Symmetries. *Phys. Rev. B - Condens. Matter Mater. Phys.* **2014**, *89* (24), 1–10. https://doi.org/10.1103/PhysRevB.89.245125.

(52) Chuntonov, L.; Haran, G. Trimeric Plasmonic Molecules: The Role of Symmetry. *Nano Lett.* **2011**, *11* (6), 2440–2445. https://doi.org/10.1021/nl2008532.

(53) Barrow, S. J.; Collins, S. M.; Rossouw, D.; Funston, A. M.; Botton, G. A.; Midgley, P. A.; Mulvaney, P. An Electron Energy Loss Spectroscopy Investigation Into Symmetry in Gold Trimer and Tetramer Plasmonic Nanoparticle Structures. *ACS Nano* **2016**, *10*, 8552–8563. https://doi.org/10.1021/acsnano.6b03796.

(54) Pacheco-Peña, V.; Beruete, M.; Fernández-Domínguez, A. I.; Luo, Y.; Navarro-Cía, M. Description of Bow-Tie Nanoantennas Excited by Localized Emitters Using Conformal Transformation. *ACS Photonics* **2016**, *3* (7), 1223–1232. https://doi.org/10.1021/acsphotonics.6b00232.

(55) Wang, F.; Shen, Y. R. General Properties of Local Plasmons in Metal Nanostructures. *Phys. Rev. Lett.* **2006**, *97* (20), 206806. https://doi.org/10.1103/PhysRevLett.97.206806.

(56) Booker, H. G. Slot Aerials and Their Relation to Complementary Wire Aerials (Babinet's Principle). *J. Inst. Electr. Eng. - Part IIIA Radiolocation* **2014**, *93* (4), 620–626. https://doi.org/10.1049/ji-3a-1.1946.0150.

(57) Chien, Y. H.; Wang, C. H.; Liu, C. C.; Chang, S. H.; Kong, K. V.; Chang, Y. C. Large-Scale Nanofabrication of Designed Nanostructures Using Angled Nanospherical-Lens Lithography for Surface Enhanced Infrared Absorption Spectroscopy. *ACS Appl. Mater. Interfaces* **2017**, *9* (29), 24917–24925. https://doi.org/10.1021/acsami.7b08994.

(58) Liu, X.; Xing, X.; Li, Y.; Chen, N.; Djerdj, I.; Wang, Y. Controllable Synthesis and Change of Emission Color from Green to Orange of ZnO Quantum Dots Using Different Solvents. *New J. Chem.* **2015**, *39* (4), 2881–2888. https://doi.org/10.1039/c5nj00070j.

(59) Chandran, A.; Barnard, E. S.; White, J. S.; Brongersma, M. L. Metal-Dielectric-Metal Surface Plasmon-Polariton Resonators. *Phys. Rev. B - Condens. Matter Mater. Phys.* **2012**, *85* (8), 1–9. https://doi.org/10.1103/PhysRevB.85.085416.

TOC